AIAA Aviation Forum and ASCEND co-located Conference Proceedings
29 July - 2 August 2024, Las Vegas, Nevada
AIAA AVIATION FORUM AND ASCEND 2024

10.2514/6.2024-4524

Analysis of Feedback Mechanism in Transonic Laminar Shock Buffet on the OALT25 Airfoil

Jun Yamasaki*[1], and Sanjiva K. Lele†[1,2]
[1]*Department of Aeronautics and Astronautics, Stanford University, Stanford, CA 94305, USA*
[2]*Department of Mechanical Engineering, Stanford University, Stanford, CA 94305, USA*

A further scrutiny of flow features present in transonic laminar shock buffet is conducted towards an improved understanding of potential feedback mechanisms that have been proposed and observed. The analysis is based on high-resolution data from a wall-resolved large-eddy simulation conducted for the flow over the OALT25 laminar supercritical airfoil at a free-stream Mach number of 0.735 and angle of attack of 4°, with a Reynolds number of 10^6 based on the chord length reported by Song et al. AIAA-2024-2141. Cross-correlation analysis of this data is used to characterize the convection velocity of disturbances in different regions and their spatial distribution. To further investigate the significance of various elements of potential feedback cycles, spectral proper orthogonal decomposition is applied to a cyclic probe set that includes the near-wall dynamics. A wavenumber decomposition of the SPOD eigenvectors corresponding to the dominant dynamics is conducted, allowing for the eduction of the spatial distributions of the energetics of upstream and downstream-directed waves. An analysis using geometrical acoustics is also presented to analyze upstream signal propagation and facilitate interpretation of the feedback cycle.

I. Introduction

The phenomenon of transonic *buffet* is characterized by self-sustaining shock oscillation, and is observed on airfoils and wings for certain critical combinations of the Mach number M_∞ and angle of attack α [1, 2]. This unsteadiness is associated with shock-boundary layer interaction, which gives rise to correspondingly oscillatory variations in aerodynamic forces and moments due to the separated flow – hence a consequent response of the airframe, known as *buffeting*, arises. One reason that this problem has attracted much engineering interest is that the low-frequencies of the oscillation associated with shock buffet are sufficiently close to that of the structural modes, which raises structural/fatigue concerns for aircraft operation in the transonic flight regime [3]. These then serve as limiters on the safe flight envelope, or maneuver boundaries, for civilian and combat aircraft alike [4].

The long-standing interest in the prediction and mechanistic understanding of buffet for aeronautical applications has spawned myriad experimental and numerical investigations. Examples of the former include wind tunnel experiments over the symmetric NACA0012 [5], as well as the OAT15A [6] and RA15SC1 [7] supercritical profiles, towards the verification of numerical codes. On the computational side, buffet has been investigated using CFD approaches of varying fidelity. Given that the shock-induced flowfield oscillation is low-frequency, many studies [3, 8, 9] solve the unsteady Reynolds-averaged Navier Stokes (URANS) equations with some success in matching experimental results, although results seem to vary nontrivially with simulation choices, e.g. of the turbulence closure. Hybrid approaches between RANS and the more costly, but scale-resolving large-eddy simulation (LES), have also been employed; for example, with zonal detached-eddy simulation (DES) [10], delayed DES (DDES) [11], and improved DES (IDDES) [12]. Studies using wall-modeled LES (WMLES), wherein the outer-layer turbulence in the boundary layer is resolved, have also been conducted [13, 14], and show understandably better agreement with experimental results.

Until relatively recently, most investigations focused on the case of *turbulent buffet*, where the boundary layer upstream of the shock is turbulent. However, as aircraft development trends [15] (e.g. for a truss-braced wing configuration) seek extended laminar flow for skin friction drag reduction and fuel efficiency, the need for the elucidation of *laminar buffet* dynamics has correspondingly emerged. A transonic wind tunnel experiment with the OALT25 was conducted by ONERA, which found similarities with turbulent buffet, but with more confined and higher-frequency shock oscillation [16]. This result is reproduced in an LES study under the same conditions, and separation bubble

*Ph.D. Student, Department of Aeronautics and Astronautics, Stanford University. AIAA Student Member. (✉ junymsk@stanford.edu)
†Edwards C. Wells Professor, Department of Aeronautics and Astronautics & Department of Mechanical Engineering, Stanford University. AIAA Associate Fellow. (✉ lele@stanford.edu)

breathing at the foot of the main shock is also observed [17]. A direct numerical simulation (DNS) of laminar buffet on the V2C airfoil has shown shock structures far more intricate than the single-shock motion observed in fully turbulent buffet [18]. Under the TFAST project, laminar buffet on the supercritical laminar V2C profile has also been simulated with DDES [19, 20], URANS [21], as well as implicit LES (ILES) [22]. Wind tunnel experiments of the same have also been performed [23, 24].

A number of theories regarding the underlying mechanism of the self-sustaining shock unsteadiness have been proposed, although the subject still eludes consensus [2]. One of the earlier, and much-debated explanations is that of Lee, who proposed a feedback mechanism based on acoustic wave propagation [25]. The original version of Lee's model describes the downstream propagation of shock-induced pressure disturbances, which produce upstream-traveling acoustic waves at the trailing edge and energetically interact with the shock; the associated timescales of each segment of this process may then be used to compute a feedback loop time/frequency, and compared to results from spectral analysis (e.g. signals of integrated force coefficients) – however, agreement has been found to be mixed [2]. The existence and potential role of other paths for acoustic waves to impact the shock from the front – e.g. upstream-moving acoustic waves, or those that first propagate along the lower side, and curve along the leading edge – has also been noted [6]. The influence of the pressure-side acoustic propagation, however, has been debated; its removal with artificial solution-freezing seemed to have minimal effect on reproducing buffet in the numerical simulation of [22], calling into question its significance for establishing feedback. Experiments investigating the sensitivity of buffet to the introduction of artificial upstream-moving acoustic waves at the trailing edge also corroborate their importance relative to pressure-side propagation [26]. Relatively recently, transonic buffet has been characterized as a global instability of the flow via global stability theory [27, 28]; shock buffet onset conditions are predicted to occur due to a supercritical Hopf bifurcation, and the stability boundary is consistent with experiments. In the same study, pressure disturbances are also observed to both travel upwards along the shock, as well as downstream, around the trailing edge, and upstream on the lower side until their ultimate ingestion in the sonic zone.

Methods of modal analysis have also seen use in the further eduction of the various interplaying processes that comprise the buffet flow. Dynamic mode decomposition (DMD) applied to DNS simulations for the V2C airfoil was shown to yield a buffet-associated mode that, while exhibiting high fluctuations near the trailing edge, did not appear to be coupled to be the same; i.e. instead of a coupling with the trailing-edge acoustics, it is the flow acceleration induced by the buffet mode that causes shock motion [18]. Modal reconstruction using the low-frequency mode extracted with spectral proper orthogonal decomposition (SPOD) has been conducted on LES data for the V2C, and demonstrated the relationship of laminar buffet with boundary-layer separation and shock motion, but not separation bubble-breathing [29]. SPOD has also been conducted for the OALT25, yielding similar mode shapes to the V2C case but exhibiting airfoil geometry dependencies for frequency and amplitude [30].

Recently, Song et al. (AIAA-2024-2141) have conducted a wall-resolved LES (WRLES) calculation of transonic laminar shock buffet over the OALT25 profile [31]. In that prior work, SPOD based on the full 3D flowfield revealed low-rank behavior at three "peaks" in the eigenvalue spectrum: $St_1 \approx 0.105$, $St_2 \approx 0.554$, and $St_3 \approx 1.093$, corresponding to the shock buffet, turbulent vortex shedding, and laminar separation Strouhal numbers respectively. Visualization of the evolution of the SPOD modes revealed three possible feedback mechanisms. The first possibility is communication from behind the main shock foot to the front of the shock via upstream-moving waves above the supersonic region. A second is due to the information propagation through the boundary layer, and the third is the upstream traveling wave on the lower side of the airfoil.

This work aims to further characterize the roles of the various components of the complex buffet flow towards an improved understanding of the potential feedback mechanism. We begin in Sec. II by recalling some aspects of the numerical simulation that was conducted to generate the high-resolution, unsteady 3D data that is analyzed in this work. In Sec. III, statistical data analysis is conducted to characterize the propagation of disturbances whose roles in the buffet cycle have been discussed. In Sec. IV, we present results for the modal decomposition of the flow state sensed along a near-wall probe set, which allows a closer focus on the more "active" region of the potential feedback cycle. Low-rank dynamics are extracted using SPOD, and a further wavenumber decomposition is conducted of these eigenmodes to educe the spatial distribution of the energies of the differently-directed waves. Finally, in Sec. V, we introduce some preliminary results regarding a geometrical acoustics approach to elucidating the interaction and possible coupling between sound propagation and shock dynamics.

II. Numerical Simulation Setup

In this investigation, we use the high resolution data of transonic flow past the OALT25 supercritical airfoil, the details of which have been given in a previous work by Song et al. AIAA-2024-2141 [31] and are summarized as follows. The chord c of the OALT25 airfoil is aligned in the x-direction, and the context is set to that of a freestream Mach number of $M_\infty = U_\infty/a_\infty = 0.735$, angle of attack of $\alpha = 4°$, and a Reynolds number based on the chord of $Re_c = \rho_\infty U_\infty c/\mu_\infty = 10^6$. Here, U_∞ denotes the flow speed, a_∞ is the speed of sound, ρ_∞ is the density, and μ_∞ is the dynamic shear viscosity, all in the freestream. The numerical calculation is of the fully compressible Navier-Stokes equations via the WRLES approach, and the primitive variables ρ, u_i, and T are the filtered density, velocity, and temperature that are in the resolved scales. By the Boussinesq hypothesis [32], the subgrid-scale (SGS) model is incorporated into the transport terms. Here the SGS eddy viscosity and thermal diffusivity are respectively computed based on the Vreman model [33] and the constant Prandtl number model. The fluid is assumed to be calorically perfect, and obeys the ideal gas equation of state, $p = \rho RT$; the freestream speed of sound is then $a_\infty = \sqrt{\gamma RT_\infty}$, with R being the specific gas constant, γ as the ratio of specific heats, and T_∞ denoting the freestream value of the temperature.

An O-type body-fitted curvilinear mesh is used, and the mesh size is $420 \times 3072 \times 512$ in the radial, azimuthal, and spanwise directions. The domain is periodic in the spanwise direction, with size $0.25c$. In the xy-plane, the domain has a radius of $R_{dom} = 70c$, with a sponge layer from a radius of $R_{spg} = 50c$. The radius of the LES region is $R_{LES} = 1.55c$, within which a hybrid central-Riemann flux with the explicit SGS model is used. Beyond R_{LES}, a pure Riemann flux, calculated using an upwind-based shock-capturing scheme, is applied. The simulation uses 6th-order compact finite difference methods [34] with collocated-staggered discretization for high spectral resolution and numerical robustness [35]. Localized central-Riemann fluxes with the weighted essentially non-oscillatory (WENO5-Z) interpolation scheme [36] is applied for shock capturing. The activation of the shock-capturing scheme is controlled by the modified Ducros sensor. The numerical dissipation imposed in the simulation, especially in the turbulent flow regime, is minimal compared to the dissipation imposed by the SGS model [35].

III. Signal Processing

To investigate the dynamics and interactions that occur near the wall, we place numerical probes at every point along a grid line that is of constant elevation away from the airfoil surface – in this case, with an airfoil-normal extrusion of $\Delta y_n/c = 0.01$ as is shown in Figure 1(a). The extracted pressure signal is displayed as an $x - t$ diagram in Figure 1(b), and one may visually confirm the various flow features present. The frontal compression wave of the λ-shock structure is present around the range $0.2 < x/c < 0.3$. The flow transitions to turbulence at around $x/c \approx 0.5$, and we observe the turbulent flow region from $x/c > 0.6$. We also note that the region in $0.5 < x/c < 0.7$ contains the main shock position variation (which has a mean position of $x/c \approx 0.55$), in addition to the supersonic pocket and terminating shock that form due to the periodic expansion regions that accelerate the flow. These regions are consistent with the observations by Song et al. [31], who described the dynamics in more detail. Note that in the plots, we have defined the x-coordinate such that it wraps around the airfoil in the clockwise direction.

Cross-correlations are calculated for the fluctuations of the pressure signal as

$$R_{nm}(\tau) = \frac{\langle p'_n(t) p'_m(t+\tau)\rangle}{\sqrt{\langle p'^2_n(t)\rangle \langle p'^2_m(t)\rangle}} \tag{1}$$

where the subscript m refers to a location within a certain chosen range, the subscript n denotes the reference location (in the middle of that spatial range) that it is cross-correlated with, and $\langle\cdot\rangle$ denotes statistical average. The fluctuating quantities are obtained via Reynolds decomposition of a flow variable (e.g. pressure) into its mean and fluctuating parts, where the former is taken over the time range of the data as well as the spanwise direction. The resulting cross-correlations are also normalized and spanwise-averaged. For ease of viewing, in Figure 2 we present a zoomed-in view with the time axis being limited to delays of $|\tau U_\infty/c| \lesssim 10$, although the entire available pressure data (8192 snapshots after excluding* the data from $tU_\infty/c \lesssim 39$) was used for the actual calculation. After obtaining the pressure correlations for each range of interest, the convection velocity is found via a line fit to the ridges of maximum correlation, representing the optimal time delay for each spatial separation.

The cross-correlation analysis was conducted for 5 ranges. In Figure 2(a) we examine the range $0 \le x_m/c \le 0.16$, with $x_n/c = 0.08$, representing a point on the suction surface near the leading edge, and upstream of the frontal

*In the early part of the data ($tU_\infty/c \lesssim 39$) some drift away from the bulk of the pressure signal was observed. Though this could be due to real intermittent behavior, we would require much longer data to process it, hence its exclusion from this present analysis.

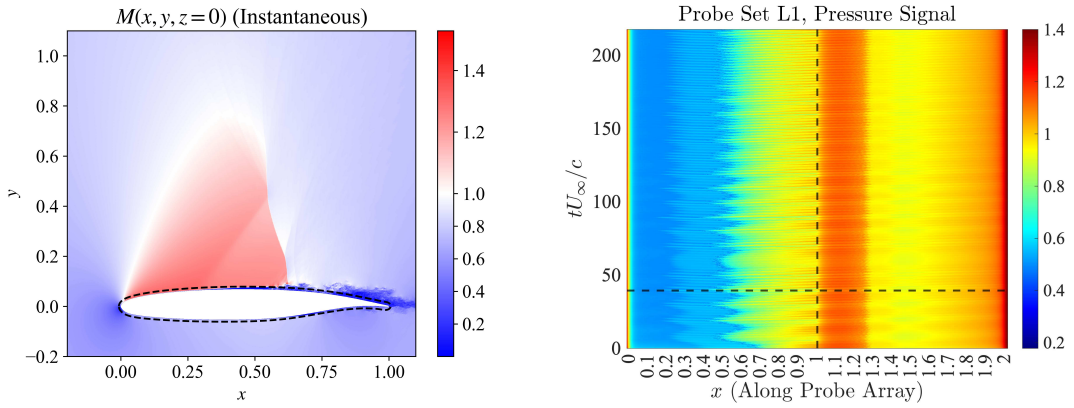

(a) Probe Set "L1" Location **(b) Pressure $x-t$ Diagram**

Fig. 1 Location of Probe Set "L1" relative to the airfoil (dashed black curve) overlayed on instantaneous Mach number at the $z = 0$ slice, and associated pressure signal (normalized by p_∞) collected on the surface as an $x-t$ diagram. The vertical dashed line in (b) indicates the location where the probe set wraps to the lower side of the airfoil. Data from the horizontal dashed line and above ($39 \lesssim tU_\infty/c \lesssim 217$) is used for the cross-correlation calculation.

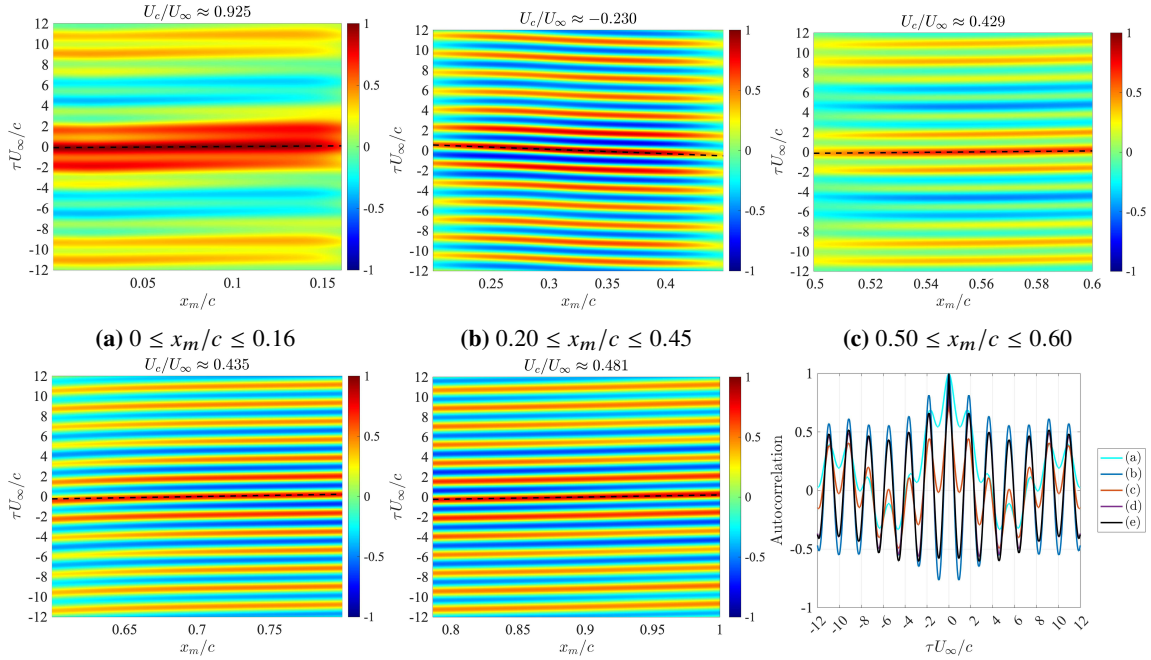

(a) $0 \le x_m/c \le 0.16$ **(b)** $0.20 \le x_m/c \le 0.45$ **(c)** $0.50 \le x_m/c \le 0.60$

(d) $0.60 \le x_m/c \le 0.80$ **(e)** $0.80 \le x_m/c \le 1$ **(f) At each reference x_n/c**

Fig. 2 Pressure cross-correlations at 5 different ranges along the upper side of Probe Set "L1". Subplot (f) represents a transverse "slice" of subplots (a)-(e) at each of the reference locations. The dashed lines in (a)-(e) correspond to the linear fits.

branch of the λ-shock; a downstream-directed convection velocity of $U_c = 0.925U_\infty$ is observed. Figure 2(b) shows the range $0.20 \le x_m/c \le 0.45$ with $x_n/c = 0.33$, which is downstream of the front branch of the λ-shock, where upstream-moving waves with a negative convection velocity of $U_c = -0.230U_\infty$ are observed. Figure 2(c) shows correlations with $x_n/c = 0.55$, and $0.5 < x_m/c < 0.6$, within the mean shock location variation but preceding the turbulent flow region. We observe a convection velocity of $U_c = 0.429U_\infty$, attributable to shock-induced disturbances.

The convection velocity of these downstream-moving disturbances measured here seems to accelerate, with the next set of ranges (shown in Figure 2(d)-(e)) exhibiting convection velocities of $U_c = 0.435U_\infty$ and $U_c = 0.481U_\infty$, respectively. We note that this acceleration has also been observed in experiments, near approximately 75% chord, in contrast to the case of turbulent buffet on the same airfoil [16]. We also present in Figure 3(b) cross-correlation conducted within the range spanning from the mean shock location to the trailing edge, yielding a time delay for downstream propagation of $\Delta\tau U_\infty/c \approx 1.435$. Additionally, from Figure 3(a) we may note the comparative strength of these disturbances detected in the cross-correlation. Notably, the signal in region (a) of Figure 2 is considerably smaller (at least by an order of magnitude), judging from its root-mean-square value.

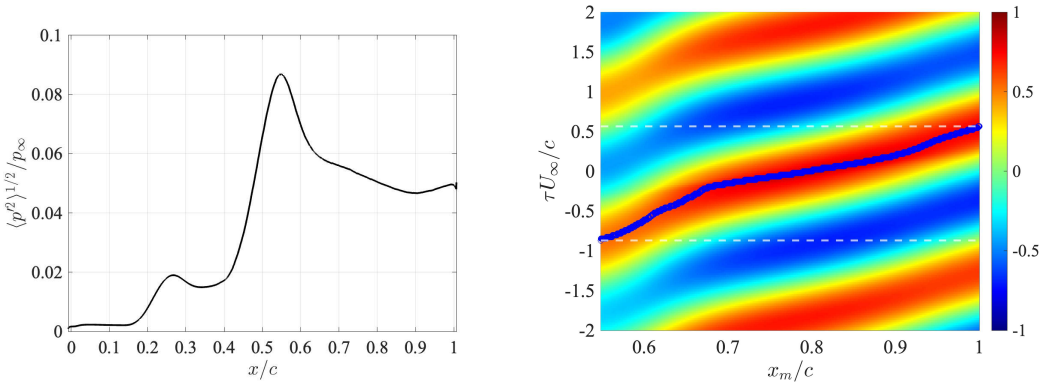

(a) Root-mean-square pressure **(b)** $0.55 \leq x_m/c \leq 1$

Fig. 3 Additional characterization of pressure fluctuation intensity along cross-correlation locations, and a longer-range cross-correlation from the mean shock location to the trailing edge. The blue markers in 3(b) are the identified optimal time delays for each spatial separation. Note that the plot is zoomed-in to $|\tau U_\infty/c| \leq 2$.

In Figure 2(f), we present an isolated view of the correlations at each of the reference locations x_n/c corresponding to the midpoint of the ranges in plots (a)-(e), as a function of the time delay. The overlayed correlation profiles show signatures of modulated oscillations, and appear in some cases to contain multiple timescales. For instance, towards the leading edge and upstream of the λ-shock, “bands" of strong correlation appear approximately every 10 convective time units (1 CTU = c/U_∞). Proceeding downstream, we see in (b) that in addition to this lower frequency, a higher-frequency oscillation emerges, which remains further downstream, e.g. after the main shock and into the turbulent region. While cross-correlation analysis allows for the estimation of convection velocities of passing disturbance signals, the multi-frequency content of these coherent motions calls for a deeper analysis of the amplitude and phase variations of these disturbances, e.g. via modal decomposition.

IV. Modal Decomposition

A. Spectral Proper Orthogonal Decomposition

With basic statistical features near the wall considered, we now move to the application of SPOD to extract coherent structures from the data measured on the probe array. We again remark that SPOD using the full data has been conducted by Song et al. [31] with the pressure, weighted dilatation, and enstrophy norms. In contrast, in this work our objective is not to find a representation of not the full flow, but instead of the dynamics in the near-wall region, where many of the active elements of the complex interactions are expected to be captured in the probe signals.

The method of SPOD is a data-driven approach that seeks to find a space-time orthogonal basis that optimally represents the data in the sense of a norm of choice [37, 38]. A key component of the method is the solution of the spectral eigenvalue problem for the eigenvalue $\lambda(St')$ and eigenfunction $\boldsymbol{\psi}(\boldsymbol{x}, St')$,

$$\iint_\Omega \boldsymbol{S}(\boldsymbol{x}, \boldsymbol{x}', St')\boldsymbol{W}(\boldsymbol{x}')\boldsymbol{\psi}(\boldsymbol{x}', St')d\boldsymbol{x}' = \lambda(St')\boldsymbol{\psi}'(\boldsymbol{x}, St') \tag{2}$$

for each frequency, where Ω is the flow domain (e.g. the probe set), $\boldsymbol{S}$ is the cross-spectral density tensor, and $\boldsymbol{x} \in \Omega$ represents a point in the flow. The obtained eigenmodes $\boldsymbol{\phi}(\boldsymbol{x}, t) = \boldsymbol{\psi}(\boldsymbol{x}, St') \exp(i2\pi St' t U_\infty/c)$ are then mutually

orthogonal in the full space-time inner product

$$\langle \boldsymbol{q}_1, \boldsymbol{q}_2 \rangle = \int_{\mathbb{R}} \iiint_{\Omega} \boldsymbol{q}_1^H(\boldsymbol{x}, t) \boldsymbol{W}(\boldsymbol{x}) \boldsymbol{q}_2(\boldsymbol{x}, t) d\boldsymbol{x} dt \tag{3}$$

where $\boldsymbol{q}$ is a state vector containing the stacked primitive variables' fluctuations (denoted by primes), i.e. $\boldsymbol{q} = [\rho', u', v', w', T']^T$, where ρ is the density, u_i are the velocity components, and T is the temperature (note that with this representation of the primitive state, the pressure disturbance p' may be recovered from the linearized equation of state); H denotes the Hermitian conjugate. Here we are reminded that we must choose a norm to define the weight function $\boldsymbol{W}$. Among the various norms that are used in practice in the definition of the inner product, we elect to use the compressible energy norm of Chu [39], which incorporates the interrelationships between the different disturbance variables and modes. Using the overline to denote the mean in the Reynolds decomposition, Chu's disturbance energy may be written as

$$E = \iiint_{\Omega} \left[\frac{1}{2} \overline{\rho} u_i' u_i' + \frac{\overline{p} \rho'^2}{2\overline{\rho}^2} + \frac{\overline{\rho} R T'^2}{2\overline{T}(\gamma - 1)} \right] d\boldsymbol{x} \tag{4}$$

so that the weight (omitting the 1/2 factor) may be defined as

$$\boldsymbol{W}(x) = \int_{\Omega_{probes}} \mathrm{diag}\left(\frac{\overline{p}}{\overline{\rho}^2}, \overline{\rho}, \overline{\rho}, \overline{\rho}, \frac{\overline{\rho} R}{\overline{T}(\gamma - 1)} \right) dx \tag{5}$$

for the case of our probe set Ω_{probes}. Note that in the discrete formulation of the inner product, the weight function definition encompasses *both* the energy and quadrature weights. In our current implementation, a simplification is made in that each probe's "volume" is weighed equally, and we do not consider curvilinear mesh weighting for the above integral. Another practical note is that for convergence of the spectral estimates of the cross-spectral density, SPOD computations require the use of Welch's periodogram method [40]. Here, we partition 6192 snapshots into bins of size 3072, with 87.5% overlap. We also gratefully acknowledge the SPOD implementation made publicly available by Oliver Schmidt [41], which was employed in this work[†].

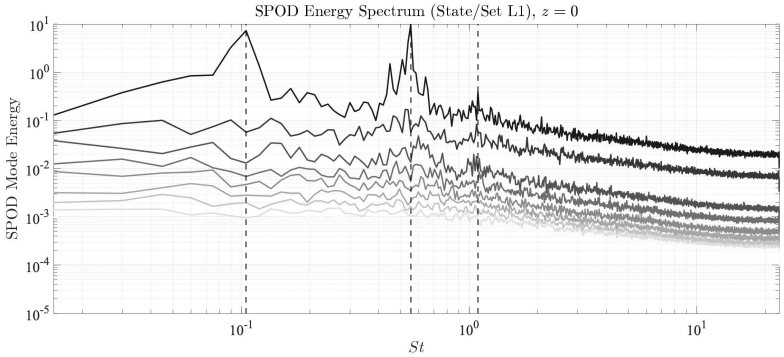

Fig. 4 SPOD energy spectrum on probe set L1. The vertical dashed lines correspond to $St_1 \approx 0.105$, $St_2 \approx 0.554$, and $St_3 \approx 1.093$. The color diminishes from the leading eigenvalue onwards.

Three peaks in the SPOD energy spectrum of Figure 4 are identified where low-rank behavior is observed. We note that the Strouhal numbers corresponding to these peaks, i.e. $St_1 \approx 0.105$, $St_2 \approx 0.554$, and $St_3 \approx 1.093$, are the same as those previously obtained in the SPOD calculation performed on the full, 3D data [31], where they were associated with buffet, turbulent vortex shedding, and laminar separation. We may then take the leading SPOD mode and investigate more closely the eigenfunctions $\boldsymbol{\psi}_{1,\chi}(x, St_k)$, where the subscript 1 denotes the leading eigenvalue, χ denotes a flow variable of interest, and k indexes the three identified Strouhal numbers. The movement of the SPOD modes may be visualized[‡] by recalling the earlier expression for the eigenmodes, and displaying the real part, i.e. $\Re\{\boldsymbol{\psi}_{1,\chi}(x, St_k) \exp(i2\pi St_k t U_\infty / c)\}$ over a period defined by $1/St_k$, and a corresponding phase $\varphi \in [0, 2\pi)$.

Such visualizations of the SPOD modes exhibit both upstream and downstream-traveling disturbances, which motivate a further decomposition of these low-rank representations of the dynamics in wavenumber space. Indeed, we

[†]As a clarification, we note that the aforementioned full SPOD in Song et al. AIAA-2024-2141 was conducted using a custom-developed code.

[‡]Animations of the spatiotemporal evolution may be accessed here.

proceed with a filtering of the SPOD modes for each of the state variables into their positive ($k_x > 0$) and negative wavenumber ($k_x < 0$) components – an analogous approach has been previously employed in studies of jet screech feedback [42, 43]. Note that here, based on the "wrapping" of the x-coordinate, the positive and negative wavenumber components would correspond to clockwise and counterclockwise propagating waves on the cyclic probe array. An inverse Fourier transform may then be applied to recast the direction-decomposed disturbance signals individually in physical space. The addition of these, along with the DC term ($k_x = 0$) can be confirmed to reproduce the original signal in physical space if windowing[§] is not used. Additionally, the spatial distribution of the energy/variance $E^{\pm}$ associated with these components, as well as their phases $\varphi^{\pm}$ may also be investigated via this wavenumber filtering.

The described analysis is shown in the next three sections for each of the representative Strouhal numbers. Certain regions in the following plots have been shaded to aid in interpretation of the results, and the abscissa is chosen to be the arc length s along the probe set for display. The blue region ($0.2 \leq x/c \leq 0.3$ or $0.23 \leq s/c \leq 0.33$) represents the approximate region where the front branch of the λ-shock is present; the orange region ($0.5 \leq x/c \leq 0.7$ or $0.53 \leq s/c \leq 0.73$) encompasses the main shock foot, as well as the periodic formation of the expansion region and terminating shock; the purple region ($0.6 \leq x/c \leq 1.01$ or $0.63 \leq s/c \leq 1.05$, overlapping with the previous) is the turbulent flow region. Beyond the final purple vertical line, the coordinate wraps to the lower surface.

B. Buffet Mode

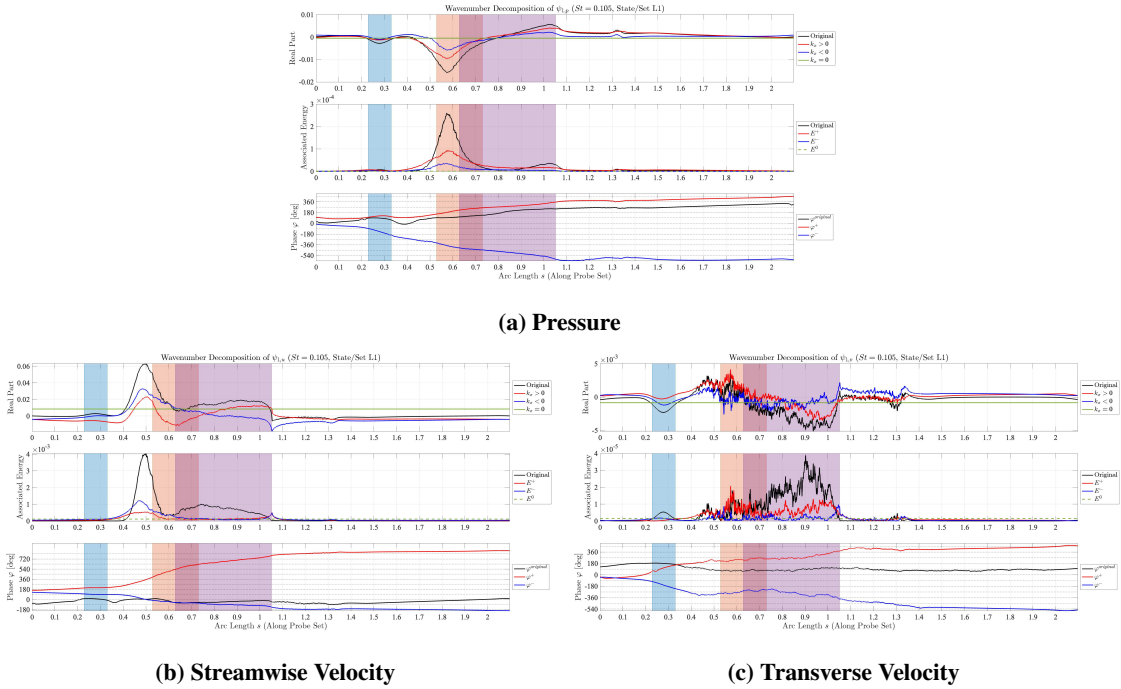

(a) Pressure

(b) Streamwise Velocity

(c) Transverse Velocity

Fig. 5 Visualization of SPOD mode decomposition (via real part), spatial distribution of decomposed energy $E^{\pm}$ and phase $\varphi^{\pm}$ for $St_1 \approx 0.105$.

The wavenumber decomposition of the leading SPOD mode at the shock buffet Strouhal number $St_1 \approx 0.105$ into its clockwise[¶] (+) and counter-clockwise (-) directed component is shown in Figure 5. For the pressure disturbance, the energy of the original SPOD mode is concentrated in the region of the main shock, as are both upstream and downstream-moving components; however, the associated energy for the downstream-directed wave is around double of the former. For the streamwise velocity, the peak of the energies is found to be in the region between the laminar separation and main shock foot location, with a higher upstream-moving component. The transverse velocity shows a stronger peak for the downstream-directed wave in the main shock region. However, we note that the transverse and

[§]Windowing would be necessary for a probe set that is truncated, e.g. only spanning 5-95% chord, but here the probe set "L1" is cyclic in space.

[¶]Again, due to the cyclic coordinate, the + wave corresponds to downstream-moving on the upper side and upstream-moving on the lower side, and vice versa for the - wave.

spanwise velocities are an order of magnitude lower than that of the streamwise component, and that a similar analysis using the full spanwise data on the probe sets to educe the z-direction modes may be more illuminating. We also remark that in all of the variables, there seems to be little energetic activity in the shock buffet-related mode on the lower side of the airfoil compared to the upper side; this suggests the limited role, if any, of the pressure-side acoustic communication in the low-frequency mode, at least in this near-wall region.

C. Turbulent Vortex Shedding Mode

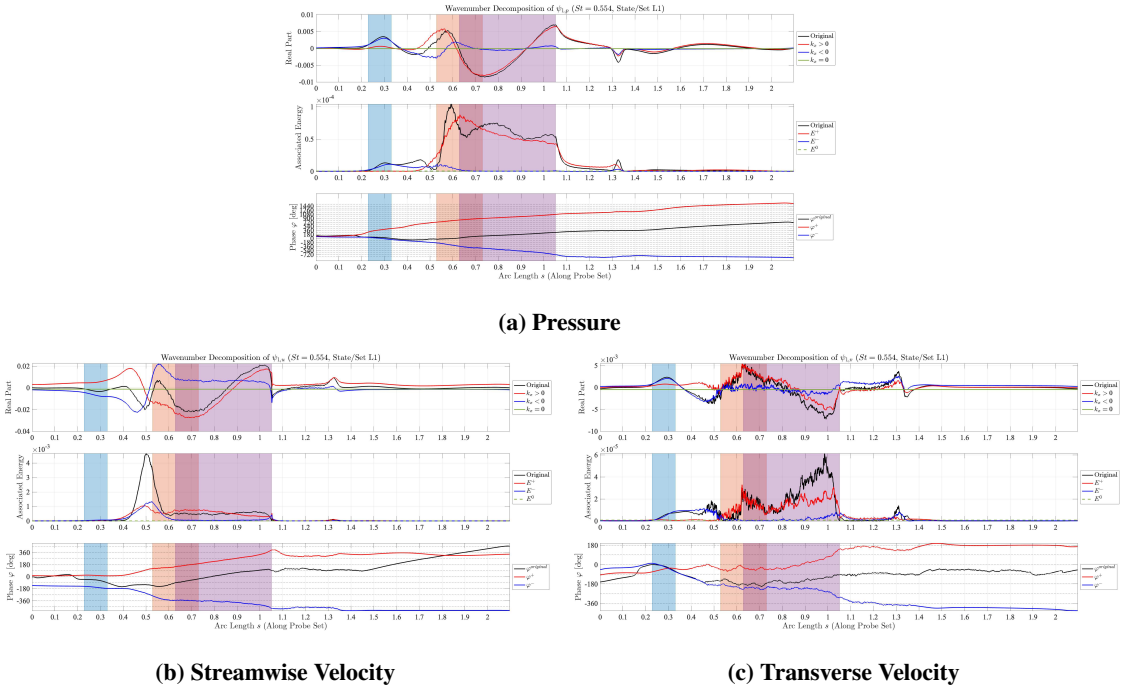

(a) Pressure

(b) Streamwise Velocity

(c) Transverse Velocity

Fig. 6 Visualization of SPOD mode decomposition (via real part), spatial distribution of decomposed energy $E^{\pm}$ and phase $\varphi^{\pm}$ for $St_2 \approx 0.554$.

Next, the leading eigenmode associated with turbulent vortex shedding, with $St_2 \approx 0.554$, is examined in Figure 6. For the pressure component, the energy is mostly captured in the downstream-directed mode, with a reduced but non-negligible portion of it still persisting until approximately 30% chord measured from the trailing edge; in contrast, the upstream-directed mode has a far diminished contribution to the overall dynamics of this St_2 mode, although slight energetic activity is identified near the main shock foot, and the preceding region up to the frontal λ-shock branch. An interesting observation is that the streamwise velocity mode appears to be peaked in between the extent of the laminar separation region and the main shock foot, for both upstream and downstream-moving components. As expected from the signal processing in the previous section, the transverse velocity is mostly dominated by its downstream-moving component, and is mostly energetic after the main shock, particularly in the fully turbulent shear layer.

D. Laminar Separation Mode

Similarly to the observations in the SPOD conducted on the full flowfield [31], we first remark that the separation at $St_3 \approx 1.093$ to the next eigenvalue is less compared to the peaks at St_1 and St_2, as may be recalled in Figure 4. In Figure 7, we see that the pressure component of this leading mode is peaked in the main shock region, within which the decomposition reveals the clear dominance of the downstream-moving part. Interestingly, the streamwise velocity component shows that the energy associated with upstream-directed disturbances is concentrated between the laminar separation and the main shock region. On the other hand, downstream-traveling disturbances have a spatial energy distribution that peaks after the start of the turbulent region; the switchover between these profiles occurs at around the mean shock location.

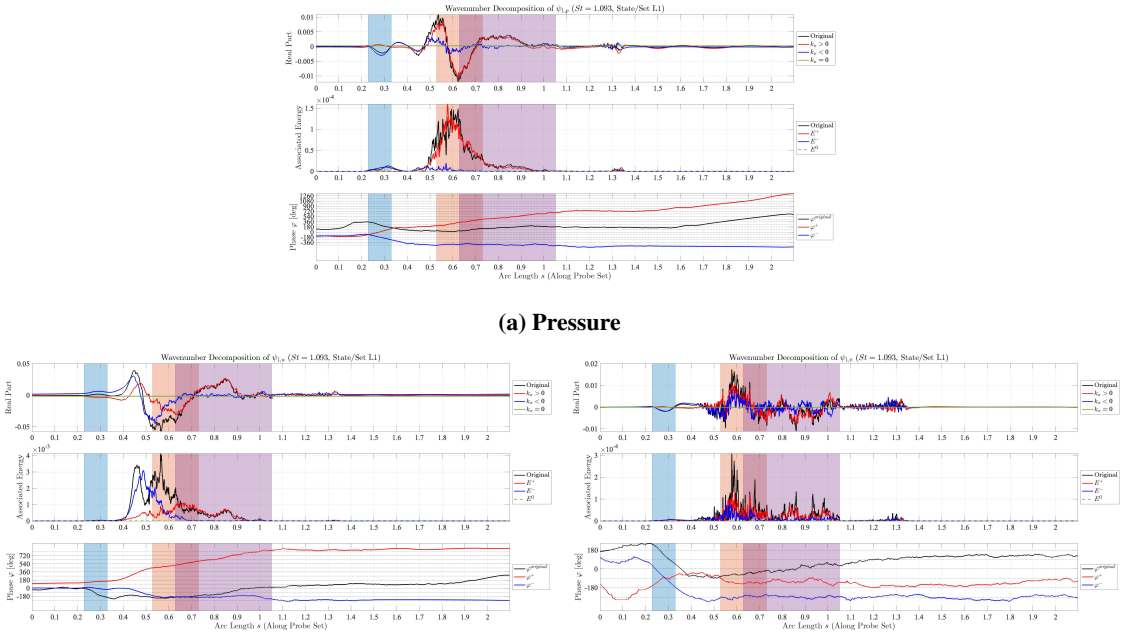

(a) Pressure

(b) Streamwise Velocity

(c) Transverse Velocity

Fig. 7 Visualization of SPOD mode decomposition (via real part), spatial distribution of decomposed energy $E^{\pm}$ and phase $\varphi^{\pm}$ for $St_3 \approx 1.093$.

V. Geometrical Acoustics

Using the results of the signal processing conducted in Sec. III, we may discuss the corresponding acoustic propagation time to verify the validity of the classic acoustic feedback explanation of Lee [25]. As an estimate for the downstream convection time, we use the results of Figure 3(b), where we found the time delay corresponding to a disturbance traveling from the mean shock location to the trailing edge to be $\Delta\tau U_\infty/c \approx 1.435$. From previous analysis of the power spectral density of the velocity dilatation signal, the shock oscillation Strouhal number was found to be $St \approx 0.1$ [31]. Therefore, if the acoustic feedback mechanism indeed holds, we expect the time delay corresponding to acoustic propagation from the trailing edge to the shock to be approximately $\tau_a \approx 8.565c/U_\infty$.

The implication of this result may be interrogated further via geometrical acoustics, an approach which has previously been taken by Memmolo et al. in their numerical investigations for the V2C airfoil [22, 44]. To trace the ray trajectories, we integrate the coupled system of ordinary differential equations [45],

$$\frac{d\boldsymbol{x}}{dt} = \frac{a^2\boldsymbol{s}}{\Omega} + \boldsymbol{v} \tag{6}$$

$$\frac{d\boldsymbol{s}}{dt} = -\frac{\Omega}{a}\nabla a - \boldsymbol{s}\times(\nabla\times\boldsymbol{v}) - (\boldsymbol{s}\cdot\nabla)\boldsymbol{v} \tag{7}$$

where $\boldsymbol{x}$ is the ray position, $\boldsymbol{s}$ is a wave-slowness vector that is perpendicular to the wavefronts, $\boldsymbol{v}$ and a are the local fluid velocity and speed of sound, and the variable $\Omega = 1 - \boldsymbol{v}\cdot\boldsymbol{s}$. As a first pass, the ray trajectories are computed on a base flow created from the spanwise and time-mean field of the entire data. Thus, the shock structure is "smeared" over its range of movement ($0.5 \lesssim x/c \lesssim 0.6$), with the flow transitioning to subsonic more smoothly over this "width" vs. discontinuously in an instantaneous snapshot, where the actual shock structure is present. Also, with the high-frequency assumption of geometrical acoustics, a problem that arises in the calculation of ray trajectories from the trailing edge is the presence of the shear layer. Here, we again refer to the approach of Memmolo [44], and launch rays from an initial wavefront that assumes propagation through a uniform flow with the freestream properties. The initial angular spacing is $\Delta\theta = 1°$, and rays are launched in all 360°, where the angle is measured from the $+x$ axis. Once regions with large gradients are escaped, the ray-tracing equations are integrated using the values on the created wavefront as the initial conditions.

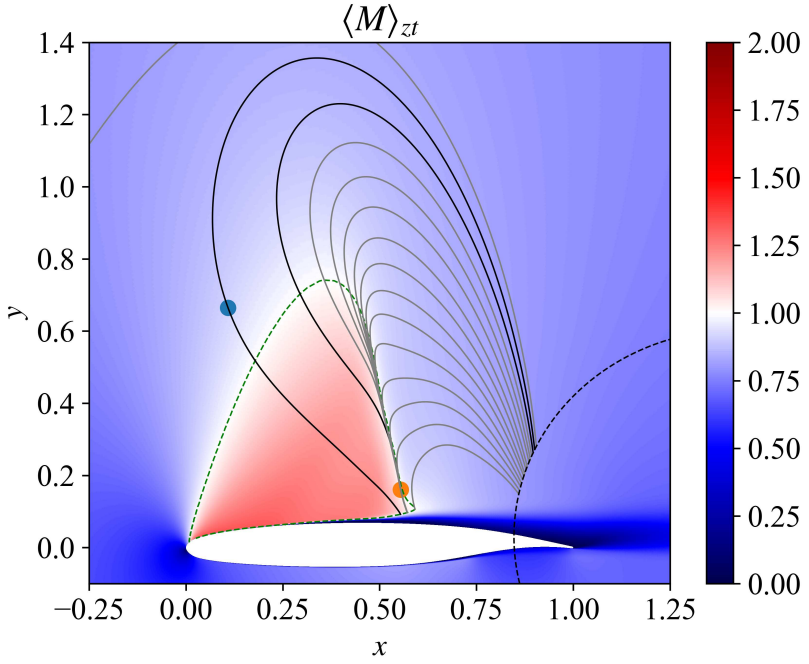

Fig. 8 Ray-tracing results displaying the trajectories that impact the shock region; the initial angular spacing is $\Delta\theta = 1°$. The dashed black line represents the initial wavefront after which the local values are sampled. The dashed green line represents the boundary of the supersonic region. The blue and orange circles mark the ray locations at the acoustic time delay under the assumption of Lee's theory, along the $\theta = 155°$ and $156°$ rays, respectively (which are in darker black). The base flow was spanwise and time-averaged across all available snapshots.

The rays that impact the shock region (in the mean flow) are found to be those initialized with angles $\theta \in [155°, 168°]$, and are isolated in Figure 8. Rays that interact from the back side of the shock, as well as those that enter from above the supersonic region and impact it from the front are observed. A key question is which of these rays corresponds to the "expected" time delay under the assumption that the acoustic feedback mechanism holds. Correspondingly, we find that the aforementioned "remaining" $\tau_a \approx 8.565c/U_\infty$ of the feedback loop time is found to be within the propagation times for the $\theta = 155°$ and $\theta = 156°$ rays, which are respectively the left and second-from-left of the bolded overarching rays.

While we have been able to observe the presence of rays that are consistent with the "expected" acoustic timescale, the results are preliminary and we reiterate that this approach has been applied on the mean flow, which is of course not what is "felt" by the propagating sound. For further clarification, it will be necessary to probe signals along these potential feedback-associated ray paths, and confirm if the spatiotemporal correlation is consistent with propagating acoustic waves. We also again note the inherent limitation of geometrical acoustics to slowly varying base states. In the present problem at $St \approx 0.1$, an order of magnitude estimate using the freestream value of the speed of sound yields a corresponding wavelength-to-chord ratio of $\lambda/c \approx 13.6$, indicating *slower* acoustic variation compared to the lengthscale of the medium. Even in cases where the high-frequency limit is not met, however, geometrical acoustics has been shown to still yield useful insights, as evidenced in investigations of jet screech [46] – furthermore, it has been shown that the solutions of the ray-tracing equations also describe wavefronts of sharp compression waves [47], calling for further scrutiny of the trailing edge pressure signal in the present data. Additionally, we note that a calculation based on the Blokhintzev invariant [45, 48] may shed quantitative insights on the amplification that we may qualitatively observe in Figure 8, where certain regions along the shock experience ray focusing. Such analyses, particularly applied to base flows corresponding to different time instants, or unsteady ray-tracing, may prove useful in illuminating the effect of the acoustic waves' interaction on the shock dynamics, as well as the potential temporal variation thereof – implementation of these ideas constitute current ongoing work.

VI. Conclusion

In this work, we have conducted further analysis on high-resolution data from a previous WRLES calculation conducted for transonic laminar buffet over the OALT25 airfoil. Following the statistical characterization of information propagation sensed in the near-wall region, we apply SPOD to decompose the dynamics into modes that optimally represent the disturbance energy contained within the local data. A wavenumber filtering approach is taken to elucidate the distribution of the energies associated with the upstream and downstream-convecting signals. Finally, we discuss the consistency of the classical acoustic feedback mechanism with the buffet frequency obtained from spectral analysis. For the downstream propagation segment the results of the signal processing are used, and the ray-tracing equations are solved to illustrate routes of potential acoustic communication between the trailing edge and shock dynamics. Finally, further potential extensions of geometrical acoustics in examining this coupling, e.g. analysis of acoustic signal amplification via the Blokhintzev invariant, are mentioned as topics for future investigation.

Acknowledgments

This material is based on work supported by the NASA Grant and Cooperative Agreement No. 80NSSC22M0108 and National Science Foundation (NSF), grant number NSF-OAC-2103509. The simulation was supported by an INCITE allocation and run on the Summit supercomputer from the Oak Ridge Leadership Computing Facility at the Oak Ridge National Laboratory, which is supported by the Office of Science of the U.S. Department of Energy under Contract No. DE-AC05-00OR22725. J.Y. is supported by the First-Year Departmental Fellowship from Stanford Aeronautics and Astronautics, and the Ezoe Memorial Recruit Foundation (Japan) Scholarship. The OALT25 airfoil geometry is provided by ONERA. The authors are grateful to Dr. Vincent Brion for sharing the original OALT25 airfoil profile. Additionally, the authors would like to thank Hang Song, Dr. Man Long Wong, and Dr. Aditya S. Ghate for their support in setting up the analysis and their kindness in sharing the high resolution data from their WRLES study.

References

[1] Lee, B., "Self-sustained shock oscillations on airfoils at transonic speeds," *Progress in Aerospace Sciences*, Vol. 37, No. 2, 2001, pp. 147–196. https://doi.org/10.1016/S0376-0421(01)00003-3, URL https://linkinghub.elsevier.com/retrieve/pii/S0376042101000033.

[2] Giannelis, N. F., Vio, G. A., and Levinski, O., "A review of recent developments in the understanding of transonic shock buffet," *Progress in Aerospace Sciences*, Vol. 92, 2017, pp. 39–84. https://doi.org/10.1016/j.paerosci.2017.05.004, URL https://linkinghub.elsevier.com/retrieve/pii/S0376042117300271.

[3] Iovnovich, M., and Raveh, D. E., "Reynolds-Averaged Navier-Stokes Study of the Shock-Buffet Instability Mechanism," *AIAA Journal*, Vol. 50, No. 4, 2012, pp. 880–890. https://doi.org/10.2514/1.J051329, URL https://arc.aiaa.org/doi/10.2514/1.J051329.

[4] Helmut, J., "Critical Review of Methods to Predict the Buffet Capability of Aircraft," *Advisory Group for Aerospace Research and Development (AGARD) Report*, 1974.

[5] McDevitt, J. B., and Okuno, A. F., "Static and Dynamic Pressure Measurements on a NACA 0012 Airfoil in the Ames High Reynolds Number Facility," 1985.

[6] Jacquin, L., Molton, P., Deck, S., Maury, B., and Soulevant, D., "Experimental Study of Shock Oscillation over a Transonic Supercritical Profile," *AIAA Journal*, Vol. 47, No. 9, 2009, pp. 1985–1994. https://doi.org/10.2514/1.30190, URL https://arc.aiaa.org/doi/10.2514/1.30190.

[7] Benoit, B., and Legrain, I., "Buffeting prediction for transport aircraft applications based on unsteady pressure measurements," *5th Applied Aerodynamics Conference*, American Institute of Aeronautics and Astronautics, Monterey,CA,U.S.A., 1987. https://doi.org/10.2514/6.1987-2356, URL https://arc.aiaa.org/doi/10.2514/6.1987-2356.

[8] Brunet, V., "Computational Study of Buffet Phenomenon with Unsteady RANS Equations," *21st AIAA Applied Aerodynamics Conference*, American Institute of Aeronautics and Astronautics, Orlando, Florida, 2003. https://doi.org/10.2514/6.2003-3679, URL https://arc.aiaa.org/doi/10.2514/6.2003-3679.

[9] Goncalves, E., and Houdeville, R., "Turbulence model and numerical scheme assessment for buffet computations," *International Journal for Numerical Methods in Fluids*, Vol. 46, No. 11, 2004, pp. 1127–1152. https://doi.org/10.1002/fld.777, URL https://onlinelibrary.wiley.com/doi/10.1002/fld.777.

[10] Deck, S., "Numerical Simulation of Transonic Buffet over a Supercritical Airfoil," *AIAA Journal*, Vol. 43, No. 7, 2005, pp. 1556–1566. https://doi.org/10.2514/1.9885, URL https://arc.aiaa.org/doi/10.2514/1.9885.

[11] Grossi, F., Braza, M., and Hoarau, Y., "Prediction of Transonic Buffet by Delayed Detached-Eddy Simulation," *AIAA Journal*, Vol. 52, No. 10, 2014, pp. 2300–2312. https://doi.org/10.2514/1.J052873, URL https://arc.aiaa.org/doi/10.2514/1.J052873.

[12] Zangeneh, R., "Parametric Study of Separation and Reattachment in Transonic Airfoil Flows," *AIAA Journal*, Vol. 59, No. 11, 2021, pp. 4465–4474. https://doi.org/10.2514/1.J060520, URL https://arc.aiaa.org/doi/10.2514/1.J060520.

[13] Fukushima, Y., and Kawai, S., "Wall-Modeled Large-Eddy Simulation of Transonic Airfoil Buffet at High Reynolds Number," *AIAA Journal*, Vol. 56, No. 6, 2018, pp. 2372–2388. https://doi.org/10.2514/1.J056537, URL https://arc.aiaa.org/doi/10.2514/1.J056537.

[14] Balakumar, P., Iyer, P. S., and Malik, M. R., "Turbulence Simulations of Transonic Flows over an NACA-0012 Airfoil (Invited)," *AIAA SCITECH 2023 Forum*, American Institute of Aeronautics and Astronautics, National Harbor, MD & Online, 2023. https://doi.org/10.2514/6.2023-0254, URL https://arc.aiaa.org/doi/10.2514/6.2023-0254.

[15] Gur, O., Schetz, J. A., and Mason, W. H., "Aerodynamic considerations in the design of truss-braced-wing aircraft," *Journal of Aircraft*, Vol. 48, No. 3, 2011, pp. 919–939.

[16] Brion, V., Dandois, J., Abart, J.-C., and Paillart, P., "Experimental analysis of the shock dynamics on a transonic laminar airfoil," *Progress in Flight Physics*, edited by D. Knight, Y. Bondar, I. Lipatov, and P. Reijasse, EDP Sciences, Krakow, Poland, 2017, pp. 365–386. https://doi.org/10.1051/eucass/2016090365, URL http://www.eucass-proceedings.eu/10.1051/eucass/2016090365.

[17] Dandois, J., Mary, I., and Brion, V., "Large-eddy simulation of laminar transonic buffet," *Journal of Fluid Mechanics*, Vol. 850, 2018, pp. 156–178. https://doi.org/10.1017/jfm.2018.470, URL https://www.cambridge.org/core/product/identifier/S0022112018004706/type/journal_article.

[18] Zauner, M., and Sandham, N. D., "Modal Analysis of a Laminar-Flow Airfoil under Buffet Conditions at Re = 500,000," *Flow, Turbulence and Combustion*, Vol. 104, No. 2-3, 2020, pp. 509–532. https://doi.org/10.1007/s10494-019-00087-z, URL http://link.springer.com/10.1007/s10494-019-00087-z.

[19] Grossi, F., "Physics and modeling of unsteady shock wave/boundary layer interactions over transonic airfoils by numerical simulation," Ph.D. thesis, Institut National Polytechnique de Toulouse-INPT, 2014.

[20] Szubert, D., Asproulias, I., Grossi, F., Duvigneau, R., Hoarau, Y., and Braza, M., "Numerical study of the turbulent transonic interaction and transition location effect involving optimisation around a supercritical aerofoil," *European Journal of Mechanics - B/Fluids*, Vol. 55, 2016, pp. 380–393. https://doi.org/10.1016/j.euromechflu.2015.09.007, URL https://linkinghub.elsevier.com/retrieve/pii/S0997754615300285.

[21] Sznajder, J., and Kwiatkowski, T., "Analysis of effects of shape and location of micro-turbulators on unsteady shockwave-boundary layer interactions in transonic flow," *Journal of KONES. Powertrain and Transport*, Vol. 23, No. 2, 2016, pp. 373–380. https://doi.org/10.5604/12314005.1213755, URL http://10048.indexcopernicus.com/abstracted.php?level=5&ICID=1213755.

[22] Memmolo, A., Bernardini, M., and Pirozzoli, S., "Scrutiny of buffet mechanisms in transonic flow," *International Journal of Numerical Methods for Heat & Fluid Flow*, Vol. 28, No. 5, 2018, pp. 1031–1046. https://doi.org/10.1108/HFF-08-2016-0300, URL https://www.emerald.com/insight/content/doi/10.1108/HFF-08-2016-0300/full/html.

[23] Placek, R., and Miller, M., "Wind Tunnel Tests of laminar-turbulent transition influence on basic aerodynamic characteristics of laminar airfoil in transonic flow regime," *Inst. of Aviation TR D-5.2*, Vol. 2, 2016.

[24] Placek, R., and Ruchała, P., "The flow separation development analysis in subsonic and transonic flow regime of the laminar airfoil," *Transportation Research Procedia*, Vol. 29, 2018, pp. 323–329. https://doi.org/10.1016/j.trpro.2018.02.029, URL https://linkinghub.elsevier.com/retrieve/pii/S2352146518300334.

[25] Lee, B., "Oscillatory shock motion caused by transonic shock boundary-layer interaction," *AIAA journal*, Vol. 28, No. 5, 1990, pp. 942–944.

[26] Hartmann, A., Feldhusen, A., and Schröder, W., "On the interaction of shock waves and sound waves in transonic buffet flow," *Physics of Fluids*, Vol. 25, No. 2, 2013, p. 026101. https://doi.org/10.1063/1.4791603, URL https://doi.org/10.1063/1.4791603.

[27] Crouch, J., Garbaruk, A., and Magidov, D., "Predicting the onset of flow unsteadiness based on global instability," *Journal of Computational Physics*, Vol. 224, No. 2, 2007, pp. 924–940. https://doi.org/https://doi.org/10.1016/j.jcp.2006.10.035, URL https://www.sciencedirect.com/science/article/pii/S0021999106005572.

[28] Crouch, J. D., Garbaruk, A., Magidov, D., and Travin, A., "Origin of transonic buffet on aerofoils," *Journal of Fluid Mechanics*, Vol. 628, 2009, pp. 357–369. https://doi.org/10.1017/S0022112009006673, URL https://www.cambridge.org/core/product/identifier/S0022112009006673/type/journal_article.

[29] Moise, P., Zauner, M., and Sandham, N. D., "Large-eddy simulations and modal reconstruction of laminar transonic buffet," *Journal of Fluid Mechanics*, Vol. 944, 2022, p. A16.

[30] Zauner, M., Moise, P., and Sandham, N. D., "On the co-existence of transonic buffet and separation-bubble modes for the OALT25 laminar-flow wing section," *Flow, Turbulence and Combustion*, Vol. 110, No. 4, 2023, pp. 1023–1057.

[31] Song, H., Wong, M. L., Ghate, A. S., and Lele, S. K., "Numerical study of transonic laminar shock buffet on the OALT25 airfoil," *AIAA SCITECH 2024 Forum*, 2024. AIAA-2024-2148.

[32] Boussinesq, J., *Essai sur la théorie des eaux courantes*, Imprimerie nationale, 1877.

[33] Vreman, A., "An eddy-viscosity subgrid-scale model for turbulent shear flow: Algebraic theory and applications," *Physics of fluids*, Vol. 16, No. 10, 2004, pp. 3670–3681.

[34] Lele, S. K., "Compact finite difference schemes with spectral-like resolution," *Journal of Computational Physics*, Vol. 103, No. 1, 1992, pp. 16–42. https://doi.org/10.1016/0021-9991(92)90324-R, URL https://linkinghub.elsevier.com/retrieve/pii/002199919290324R.

[35] Song, H., Ghate, A. S., Matsuno, K., West, J., Subramaniam, A., Brown, L. J., and Lele, S. K., "Robust high-resolution simulations of compressible turbulent flows without filtering," *AIAA AVIATION 2022 Forum*, American Institute of Aeronautics and Astronautics, Chicago, IL & Virtual, 2022. https://doi.org/10.2514/6.2022-4122, URL https://arc.aiaa.org/doi/10.2514/6.2022-4122.

[36] Borges, R., Carmona, M., Costa, B., and Don, W. S., "An improved weighted essentially non-oscillatory scheme for hyperbolic conservation laws," *Journal of computational physics*, Vol. 227, No. 6, 2008, pp. 3191–3211.

[37] Towne, A., Schmidt, O. T., and Colonius, T., "Spectral proper orthogonal decomposition and its relationship to dynamic mode decomposition and resolvent analysis," *Journal of Fluid Mechanics*, Vol. 847, 2018, pp. 821–867. https://doi.org/10.1017/jfm.2018.283, URL https://www.cambridge.org/core/product/identifier/S0022112018002835/type/journal_article.

[38] Schmidt, O. T., and Colonius, T., "Guide to Spectral Proper Orthogonal Decomposition," *AIAA Journal*, Vol. 58, No. 3, 2020, pp. 1023–1033. https://doi.org/10.2514/1.J058809, URL https://arc.aiaa.org/doi/10.2514/1.J058809.

[39] Chu, B.-T., "On the energy transfer to small disturbances in fluid flow (Part I)," *Acta Mechanica*, Vol. 1, No. 3, 1965, pp. 215–234. https://doi.org/10.1007/BF01387235, URL http://link.springer.com/10.1007/BF01387235.

[40] Welch, P., "The use of fast Fourier transform for the estimation of power spectra: a method based on time averaging over short, modified periodograms," *IEEE Transactions on audio and electroacoustics*, Vol. 15, No. 2, 1967, pp. 70–73.

[41] Schmidt, O. T., "Spectral proper orthogonal decomposition using multitaper estimates," *Theoretical and Computational Fluid Dynamics*, Vol. 36, No. 5, 2022, pp. 741–754.

[42] Wu, G., Lele, S., and Jeun, J., "Coherence and feedback in supersonic rectangular jet screech," *Annual Research Briefs*, Vol. 17, 2020, pp. 133–144.

[43] Jeun, J., Wu, G. J., and Lele, S. K., "A closure mechanism for screech coupling in rectangular twin jets," *Journal of Fluid Mechanics*, Vol. 987, 2024, p. A5. https://doi.org/10.1017/jfm.2024.376.

[44] Memmolo, A., "Numerical study of transonic buffet on supercritical airfoil with different boundary layer states," Ph.D. thesis, Università degli Studi di Roma" La Sapienza", 2018.

[45] Pierce, A. D., *Acoustics: an introduction to its physical principles and applications*, Springer, 2019.

[46] Manning, T., and Lele, S., "A numerical investigation of sound generation in supersonic jet screech," *6th Aeroacoustics Conference and Exhibit*, 2000, p. 2081.

[47] Suzuki, T., and Lele, S. K., "Shock leakage through an unsteady vortex-laden mixing layer: application to jet screech," *Journal of Fluid Mechanics*, Vol. 490, 2003, pp. 139–167.

[48] Blokhintzev, D., "The propagation of sound in an inhomogeneous and moving medium I," *The Journal of the Acoustical Society of America*, Vol. 18, No. 2, 1946, pp. 322–328.